AFCM-LSMA: New intelligent model based on Lévy slime mould algorithm and adaptive fuzzy C-means for identification of COVID-19 infection from chest X-ray images

Ahmed M. Anter [a,b], Diego Oliva [c], Anuradha Thakare [d], Zhiguo Zhang [a,e,*]

[a] School of Biomedical Engineering, Health Science Center, Shenzhen University, Shenzhen 518060, China
[b] Faculty of Computers and Artificial Intelligence, Beni-Suef University, Benisuef 62511, Egypt
[c] Depto. de Ciencias Computacionales, Universidad de Guadalajara, CUCEI, Av. Revolución 1500, 44430 Guadalajara, Jalisco, Mexico
[d] Pimpri Chinchwad College of Engineering, Savitribai Phule Pune University, India
[e] Marshall Laboratory of Biomedical Engineering, Shenzhen University, Shenzhen, China

ARTICLE INFO

ABSTRACT

Problem: A worldwide challenge is to provide medical resources required for COVID-19 detection. They must be effective tools for fast detection and diagnose of the virus using a large number of tests; besides, they should be low-cost developments. While a chest X-ray scan is a powerful candidate tool, if several tests are carried out, the images produced by the devices must be interpreted accurately and rapidly. COVID-19 induces longitudinal pulmonary parenchymal ground-glass and consolidates pulmonary opacity, in some cases with rounded morphology and peripheral lung distribution, which is very difficult to predict in an early stage.
Aim: In this paper, we aim to develop a robust model to extract high-level features of COVID-19 from chest X-ray (CXR) images to help in rapid diagnosis. In specific, this paper proposes an optimization model for COVID-19 diagnosis based on adaptive Fuzzy C-means (AFCM) and improved Slime Mould Algorithm (SMA) based on Lévy distribution, namely AFCM-LSMA.
Methods: The SMA optimizer is proposed to adapt weights in oscillation mode and to mimic the process of generating positive and negative feedback from the propagation wave to shape the optimum path for food connectivity. Lévy motion is used as a permutation to perform a local search and to adapt SMA optimizer (LSMA) by generating several solutions that are apart from current candidates. Furthermore, it permits the optimizer to escape from local minima, examine large search areas and reach optimal solutions in fewer iterations with high convergence speed. The FCM algorithm is used to segment pulmonary regions from CXR images and is adapted to reduce time and amount of computations using histogram of the image intensities during the clustering process.
Results: The performance of the proposed AFCM-LSMA has been validated on CXR images and compared with different conventional machine learning and deep learning techniques, meta-heuristics methods, and different chaotic maps. The accuracies achieved by the proposed model are around ($ACC = 0.96$, $RMSE = 0.23$, $Prec. = 0.98$, $F1\_score = 0.98$, $MCC = 0.79$, and $Kappa = 0.79$).
Conclusion: The experimental findings indicate that the proposed new method outperforms all other methods, which will be beneficial to the clinical practitioner for the early identification of infected COVID-19 patients.

1. Introduction

The new virus called COVID-19 was identified in Wuhan, China, in December 2019 [1]. It belongs to the Corona family of viruses, but it is more deadly and dangerous than the rest of the coronaviruses [2]. Due to the restricted testing resources available, several countries are only willing to apply the COVID-19 test to a small number of people. Despite considerable efforts to find a viable way to diagnose COVID-19, a major obstacle remains the medical services available in many countries. There is also an urgent need to identify a quick and convenient process for

effectively detecting and diagnosing COVID-19.

As the number of patients infected by this disease increases every day, it turns out to be extremely hard for radiologists to finish the diagnostic process in the constrained accessible time [3]. Medical image analysis is one of the most important fields of study, offering diagnosis and decision-making tools for a variety of diseases, such as the Middle East respiratory syndrome (MERS) or COVID-19, among others. Recently, many efforts and more attention are paid to imaging modalities. Therefore, interpretation of these images requires expertise and necessitates several algorithms to enhance, accelerate and make an accurate diagnosis [4]. There have been several attempts to find an effective and fast way to identify contaminated patients early on using image processing and artificial intelligence algorithms. For example, Randhawa et al. [5] proposed supervised machine learning techniques with digital signal processing (MLDSP) for COVID-19 detection using intrinsic genomic signatures for rapid classification of novel pathogens. Li et al. [6] developed a fully automatic framework to detect COVID-19 from chest CT using a deep learning model (COVNet). The dataset was collected from 6 hospitals to detect COVID-19 accurately and differentiate it from pneumonia and other lung diseases. Al-Waisy et al. [7] proposed a hybrid deep learning framework for identifying COVID-19 in CXR images (COVID-CheXNet). First, the contrast of the CXR image was enhanced, and the noise level was reduced. Then, the learning features obtained from two different pre-trained deep learning models are fused and used to classify and discriminate between the healthy and COVID-19 infected people. They improved their work based on CXR images for Pneumonia COVID-19 detection using a hybrid multimodal deep learning system (COVID-DeepNet) [8]. Mohammed et al. [9] present a comprehensive investigation of different machine learning for automated identification of COVID-19 from CXR using ANN, SM, RBF, k-NN, and DT and different architectures of convolutional deep learning models. Mohammed et al. [10] proposed an intelligent system to help in COVID-19 diagnosis. The multi-criteria decision-making (MCDM) method is integrated with TOPSIS for benchmarking and ranking purposes, while entropy was used to calculate the weights of criteria, and the SVM classifier was used for COVID-19 diagnosis. Abdulkareem et al. [11] developed a model to diagnose patients with COVID-19 in smart hospitals based on machine learning and the Internet of Things. They used three ML methods: Naive Bayes (NB), Random Forest (RF), and SVM for COVID-19 classification. Ismael and Şengür [12] proposed deep feature extraction, fine-tuning of pre-trained convolutional neural networks (CNN), and end-to-end training of a developed CNN model COVID-19 classification from CXR images. Nayak et al. [13], proposed different architectures of automated deep learning for the classification of COVID-19 from normal cases using chest X-ray images. The best performance is obtained by CNN-ResNet-34 with an accuracy of 98.33%. Gupta et al. [14] proposed the Stacking InstaCovNet-19 model for the detection of COVID-19 patients using CXR images. This model uses various pre-trained models to compensate for a relatively small amount of training data. From the literature review, we can confirm that the accuracy and optimum time remain a major challenge for the doctors to reduce the suffering of the patients.

When being used on X-ray based pneumonia COVID-19 diagnosis, classical machine learning (ML) techniques have faced numerous problems, such as stuck in local minima, time-consuming, sensitivity to noise, and uncertainty. The most growing and complicated issue is the curse of dimensionality. There are usually two major approaches to the feature selection: (1) the filter approach is based on some statistical criteria and assigns scores to each feature, (2) the wrapper approach is based on a heuristic search of all possible subsets of feature [15]. To improve and boost the effectiveness of feature selection, bio-inspired swarm intelligence (SI) approaches are required for global optimization [16].

SI algorithms have recently been on track to address engineering optimization issues [17]. It has demonstrated its efficiency in solving large-scale problems as well as non-linear optimization problems, which are increasingly growing in complexity in comparison to their size. All SI algorithms have differences and similarities, for example, all of them perform two steps known as exploration and exploitation. The exploration is when the algorithm is diversifying the solutions looking for prominent regions in the search space. Meanwhile, in the exploitation, the searching is intensified but only in the areas detected by the exploration. The balancing between these two phases is the key challenge to achieve an adequate balance for the optimization problem [18]. Slime Mould Algorithm (SMA) is one of the more recent global SI optimization algorithms that is caused by the slime mould diffusion and foraging behavior [19]. SMA relies primarily on the spreading wave generated by the biological oscillator to adjust the cytoplasmic flow of the veins in such a way that they appear to be in a better place of food concentration. At the same time, SMA uses weights to simulate the positive and negative feedback generated during foraging and thus forming different morphotypes.

The advantages of SMA over different SI algorithms are as follows: (1) it has fewer parameters that need to adapt during the optimization process. (2) the distribution of SMA is mainly concentrated in multiple regions with local optimum, which shows the tradeoff of slime mould between multiple local optimums. (3) the fast oscillation in the exploration phase and the slight oscillation in the exploitation phase can ensure the fast convergence of slime mould and the accurate search near the optimal solution. Moreover, SMA exhibits significant advantages in the exploitation phase for uni-modal and multi-model functions and able to avoid local optimum and show better exploration. Furthermore, it achieves superior solutions faster than other counterparts due to the ability to well coordinate between exploration and exploitation [19].

However, the existing bio-inspired algorithms cannot solve all types of optimization problems. When the exploration facility is improved in SMA, it will lead to reductions in the exploitation capability, and vice versa. It is relatively challenging to attain an appropriate balance between these two phases through the optimization process, specially with the critical cases. Hence, there is a need for a new or enhanced optimization algorithms to better resolve existing problems that are too complicated to solve with current methods. Therefore, for optimization and optimum search, Lévy's distribution behavior is employed to get a good balance between the exploration and exploitation phases. The Lévy motion process is known as a non-Gaussian stochastic motion which can be considered as a random search pattern extracted from nature. In general terms, the Lévy motion is a random movement in which its duration depends on a Lévy distribution [20]. Many natural and artificial facts that can be depicted by Lévy distribution, such as fluid dynamics, earthquake analysis, and diffusion of fluorescent molecules,… etc. [21]. Lévy also was used by Ren et al. [22] and Iacca et al. [23] for constrained and non-constrained problems, and by Charin et al. [24] and Zhang et al. [25] for estimating parameters in a photovoltaic system under partial shading conditions. Lévy considers as a family of scale-free distribution by random steps and directions. Lévy helps the optimizer by generating several solutions that are different from the existing solutions to escape local minima, increase the efficiency in examining large search areas, avoid premature convergence, and improve the global search.

On the other hand, segmentation of the X-ray scans by separating regions of an image from each other is an important phase in the image processing and computer vision, focusing on a particular region, thus increasing the precision of the techniques of image analysis. One of the most common algorithms for clustering is the fuzzy c-means (FCM) [26]; it is an unsupervised learning method that is simple and can maintain more information than other methods. In medical images, the FCM has been applied in different clustering problems such as [27–32]. The main drawbacks of the FCM are that easily affected by noise and highly time-consuming. Besides, it does not consider the spatial information of the image. The adaptive-FCM has been proposed to overcome these problems; this adapted clustering method reduces the time consumption and enhances the immunity to noise. However, in an application such as pneumonia COVID-19 diagnosis, to obtain good segmented images, it is

necessary to precisely define the centroids and increase the convergence speed.

The motivation of this study is to propose an accurate diagnosis model with optimum time for COVID-19 infection from chest X-ray image depends on combining the strength of different techniques. The proposed model mainly consists of five phases; in the first phase (***Preprocessing***), the images are enhanced, and noise is removed using removal and median filters. In the second phase (***Segmentation***), pulmonary regions are segmented from a chest X-ray, the adaptive-FCM is proposed to cluster image and segment pulmonary regions from CXR images automatically. Then, the morphological operators are used to refine the segmentation process. In the third phase (***Feature extraction***), the high-level features with different scales are extracted from the segmented regions using five different feature extraction methods: Grey Level Co-occurrence Matrix (GLCM), Histogram of Oriented Gradients (HOG), Local Binary Pattern (LBP), Segmentation based fractal texture analysis (SFTA), and Speeded-Up Robust Features (SURF). Then these features are fused to increase the diversity of features and to increase the rate of classification accuracy. Feature fusion helps to learn image features fully for the description of their rich internal information and helps to obtain a compact representation of integrated features, thus resulting in lower computational complexity and better performance to identify COVID-19 with an unconstrained environment. In the fourth phase (***Feature selection***), the SMA method is adapted to determine the optimal significant features from the huge matrix of extracted features for subsequent classification and decision making. To address the increase in the performance of SMA, we propose to use Lévy motion distribution to achieve the balance between exploration and exploitation rates. Moreover, the kernel-decision-tree function is used as a part of the optimizer to validate the significant features. In the fifth phase (***Classification***), the optimal features, whose selected by LSMA after feature fusion, are used to train the decision tree classifier for recognition of COVID-19 from chest X-ray images. Moreover, different assessment criteria are used to compare the efficiency of the proposed model and the whole model (called AFCM-LSMA) with popular meta-heuristic optimization algorithms and various chaotic maps. The experimental results confirm that the proposed model can properly estimate the optimal features with fast convergence. Besides, a high accuracy is also computed in the identification of COVID-19 patients.

The main contributions of this article are listed as follow:

– An improved slime mould optimization algorithm based on Lévy distribution (LSMA) is proposed to select high-level features of COVID-19 from CXR images to help in rapid diagnosis and to improve classification accuracy.
– Lévy motion distribution is used as a permutation to perform a local search, escape from local minima, and adapt SMA optimizer.
– An improved FCM algorithm is adapted to reduce the time and number of computations in pulmonary regions segmentation from CXR images using the histogram of the image,
– The experimental results revealed that the proposed AFCM-LSMA is superior to other well-known bio-inspired optimization algorithms and different chaotic maps in the literature and outperforms different machine learning and deep learning techniques.

The remainder of this paper is organized as follows. Section 2 presents the dataset description and the background of the methods involved in the proposed model. Section 3 introduces the AFCM-LSMA model for COVID-19 X-ray diagnosis. Experimental results are presented in Section 4. Finally, Section 5 concludes this paper and presents the future work.

2. Materials and methods involved

2.1. Dataset description

The dataset is composed of 1124 CXR images. More specifically, there are 403 images of patients with COVID-19 and 721 images of normal patients. The dataset of CXR images are collected from four publicly available sources: (1) IEEE-COVID-19 CXR images [33], (2) Radiography-COVID-19 CXR images [34], (3) Initiative-COVID-19 CXR images [35], and (4) Radiopedia-COVID-19 [36]. The decision to collect and create one dataset of CXR images from four sources is motivated because each one has a limited number of CXR COVID-19 cases, and also, they are all open-source and freely transparent to the public and research communities. Samples of the selected images are given in Fig. 1.

2.2. Slime mould algorithm (SMA)

The SMA is a new optimizer that takes as inspiration the slime mould (SM) oscillation mode [19]. The slime mould relates to the physarum polycephalum, which was first identified as a fungus, and for that reason, it is called "slime mould". One of the main features of the SMA is the mathematical model that considers the use of weights that dynamically adapt their values. The weights permit to have feedback about the propagation wave of SM by using a bio-oscillator that allows to have a mechanism for linking food. This process conduces a proper balance between the exploration and exploitation of the search space.

The SM, also called plasmodium, is the primary nutritional step; it is also a dynamic phase in SM. Throughout the migration, the front end is converted into a fan-shaped network, accompanied by an integrated venous network allowing cytoplasm to circulate within. Due to their features related to the patterns, they may concurrently utilize several sources of food to create a venous network that binds them. If the environment has enough food, SM may also grow to over 900 square centimeters. For food sources, SM uses a bio-oscillator to create a propagating wave that raises the cytoplasm flow across the vein. Then most of the cytoplasm goes to the thicker section of the vein. Along the process and by using the positive–negative feedback, the slime can define an optimal path to a relatively superior food connection. The mathematical model of SM may also be developed and implemented in graph theory and route networks.

The SM can dynamically change their search patterns based on the nature of the source food. If a food source has a high-quality, then the SM employs the process called region-limited search. Considering such facts, this is the exploitation phase where the search is focused only on certain food sources. Meanwhile, if the quality of the food is low, then the SM leaves the food source and moves to another region of the search space. This corresponds to the exploration. To model SMA algorithm [19], the following equation is used to simulate the contraction mode of the approaching behavior:

$$\overrightarrow{X(t+1)} = \begin{cases} \overrightarrow{X_b(t)} + \overrightarrow{vb} \cdot \left(\overrightarrow{W} \cdot \overrightarrow{X_A(t)} - \overrightarrow{X_B(t)} \right), r < p \\ \overrightarrow{vc} \cdot \overrightarrow{X(t)}, r \geq p \end{cases} \quad (1)$$

where $\overrightarrow{vb}$ is oscillates parameter $\overrightarrow{vb} \in [-a, a]$, $\overrightarrow{vc}$ is oscillates parameter decreases linearly from [1,0], t is the current iteration, $\overrightarrow{X_b}$ represents the best position obtained so far, $\overrightarrow{X}$ denotes the current position of slime mould, $\overrightarrow{X_A}$ and $\overrightarrow{X_B}$ are two randomly selected individuals from the swarm, $\overrightarrow{W}$ denotes the weight of SM. The p parameter can be represented as follows:

$$p = \tanh|S(i) - BF| \quad (2)$$

where $i \in 1, 2, 3, \cdots, n$, $S(i)$ denotes the fitness of $\overrightarrow{X}$, BF is the best fitness
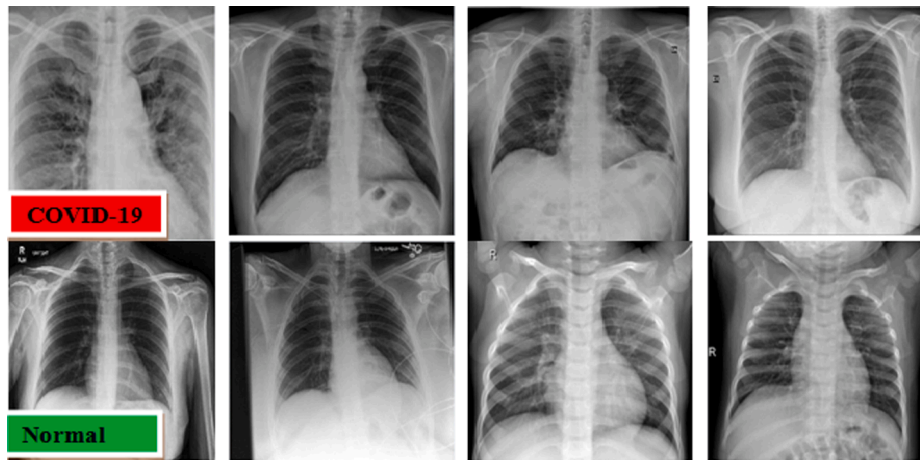
Fig. 1. Examples of X-ray scans from the collected dataset. The first row represents the COVID-19 for different infected cases and the second row represents the normal cases.

obtained so far. The parameter $\overrightarrow{vb}$ can be calculated is as follows:

$$\overrightarrow{vb} = [-a, a] \qquad (3)$$

$$a = \operatorname{arctanh}\left(-\left(\frac{t}{\max\_t}\right) + 1\right) \qquad (4)$$

The weight of SM $\overrightarrow{W}$ can be calculated as follows:

$$\overrightarrow{W(Fitness_{Min}(i))} = \begin{cases} 1 + rand \cdot log\left(\frac{bF - S(i)}{bF - wF} + 1\right), i \leq (N_{agent}/2) \\ 1 - rand \cdot log\left(\frac{bF - S(i)}{bF - wF} + 1\right), others \end{cases} \qquad (5)$$

$$Fitness_{Min} = sort(S) \qquad (6)$$

where $i \leq (N_{agent}/2)$ simulates the SM to adjust their search to the food quality and N_{agent} represents the number of agents. $S(i)$ indicates the ranks first half of the population. The *rand* is random variable $rand \in [0, 1]$, bF and wF represent the optimal and worst fitness through the current iterative process, respectively, and $Fitnes_{Min}(i)$ is the sorted sequence of minimum fitness values. Besides, Eq. (5) reflects the positive and negative feedback that exists between the width of the SM vein and the concentration of food explored. The greater the concentration of food reached by the vein, the stronger the bio-oscillator wave, the faster the cytoplasm flows, and the thicker the vein.

To update the SM position the following mathematical formula is proposed:

$$\overrightarrow{X^*} = \begin{cases} rand \cdot (U - L) + L, rand < z \\ \overrightarrow{X_b(t)} + \overrightarrow{vb} \cdot \left(W \cdot \overrightarrow{X_A(t)} - \overrightarrow{X_B(t)}\right), rand < p\overrightarrow{vc} \cdot \overrightarrow{X(t)}, rand \geq p \end{cases} \qquad (7)$$

where L and U are the limited boundaries of the search space, lower and upper, respectively. The parameter z is used to probability maintain the SMA search space for exploration and exploitation. In this paper, the optimal value for parameter z is set to 0.03.

The SM relies primarily on the spreading wave generated by the biological oscillator to adjust the cytoplasmic flow of the veins in such a way that they appear to be in a better place of food concentration. To simulate variations in the venous width of the SM, the parameters $\overrightarrow{W}, \overrightarrow{vb}$, and $\overrightarrow{vc}$ are used to identify the variations. $\overrightarrow{W}$ reflects the oscillation frequency of SM close one at various food concentrations, meaning that SM will approach food more rapidly while seeking high-quality food, thus approaching food more slowly when the concentration of food is

lower in individual positions, thereby increasing the efficiency of SM in selecting the optimum food source. To pursue a better food source, and though SM has found a better food source, it would also separate some organic matter for exploring and searching other places in an attempt to locate a higher quality food source, rather than concentrating it all in one place. The steps of SMA algorithm are shown in Algorithm 1.

2.2.1. SMA-based Lévy distribution

In the 1930s, a researcher discovered a class of probability distributions having an infinite second moment and governing the sum of these random variables. Such distribution is called Lévy motion [20]. In previous research, it is seen that the foraging behavior of nature animals is a sort of random act of movement. Since the next move usually depends on the current position and the probability of moving to the next position, the success of each random move is quite critical. Recent studies have shown that Lévy's distribution is one of the strongest methods for random movement [21]. The process is known as a non-Gaussian stochastic random motion form, in which a Lévy distribution is used to compute the random step lengths. To identify the issues in a broad range of unknown large search spaces, the variation of Lévy's movement (non-Gaussian distribution) is more efficient compared to the dimensional Brownian movement (Gaussian distribution); this efficiency motivates the optimization algorithms to use this distribution. Since this distribution has more chances to search further points than Gaussian distribution. Therefore, numerical and optimization algorithms for generating Lévy random distribution were introduced in different applications to provide a chance to escape from local optima such as [22–25].

Fig. 2 shows an example of the Lévy movements, where it is possible to see different jumps with long and short distances. In this study, the Lévy motion mechanism is introduced to the Slime mould position update. On the one hand, it can effectively avoid the overreliance of the slime mould position change on the previous generation position information and ensure the diversity of the population. On the other hand, the random oscillations mode of Lévy that changes large steps suddenly after a series of small steps gives the slime mould individual the ability to inverse suddenly to another location, which helps the algorithm to escape from the local minima, avoiding the premature convergence, increase the efficiency in examining large search area, and improve the global search capability. Besides, Lévy random motion adopts the optimizer to generate several solutions that are different from existing solutions. The mathematical model of the Lévy distribution is defined as follows:
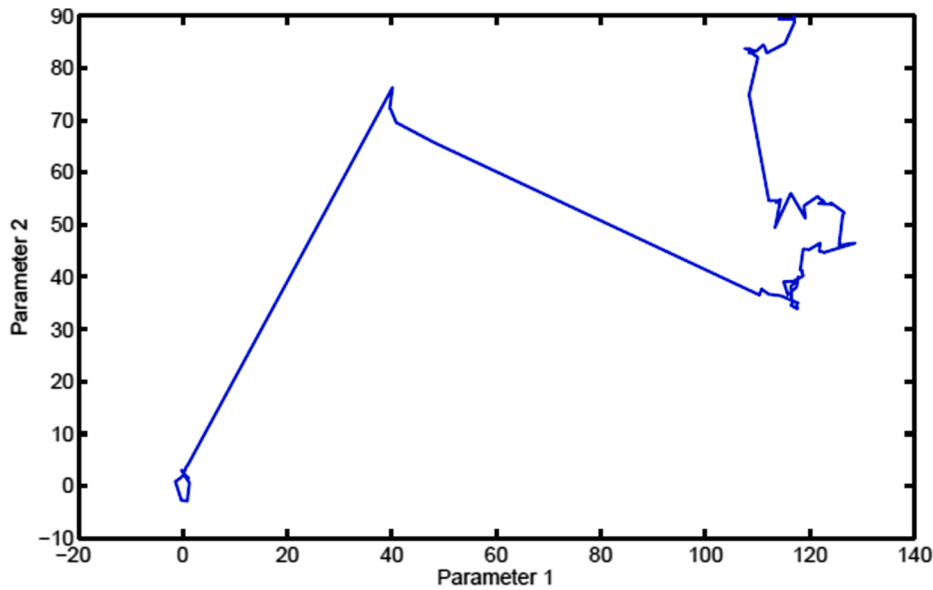
Fig. 2. A series of 100 consecutive steps of Lévy motions (non-Gaussian distribution).

$$L(s, \gamma, \mu) = \begin{cases} \sqrt{\dfrac{\gamma}{2\pi}} \exp\left(-\dfrac{\gamma}{2(s-\mu)}\right) \dfrac{1}{(s-\mu)^{3/2}}, 0 < \mu < s < \infty \\ 0 \; otherwise \end{cases} \quad (8)$$

where μ is minimal step size (shift parameter), γ is a scale parameter $\gamma > 0$, and s is a random vector computed from a simple power-law formula $L(s) \; |s|^{-1-\beta}$ where $0 < \beta < 2$. Lévy motion is more effective than Gaussian's random motion to perform the exploration of complex search spaces and it can be seen from the long and abrupt jumps. Thus, Lévy's random motion motivates to exploit it to perform the random motion of slime mould.

The SMA agents are redistributed in the search space with Lévy method. To get rid of local minima and improve the global search capability. Therefore, a new SMA position X_{i+1} corresponding to an ith SM is obtained by combining a Lévy motion with its old position X_i as follows:

$$X_{i+1} = X_i + \mathscr{L} \oplus L(\lambda) \quad (9)$$

where $\mathscr{L}$ is a random step size parameter, and λ is a Lévy motion distribution parameter. The step size $\mathscr{L}$ is achieved using the Mantegna formula as follows:

$$\mathscr{L} = v \oplus L(\lambda) \sim 0.01 \dfrac{u}{|v|^{1/B}} \left(X_i - \widehat{X}\right) \quad (10)$$

where X_i is the current position and $\widehat{X}$ is the best position obtained. The factor 0.01 comes from the fact that $\mathscr{L}/100$ should the typical step size of walks where $\mathscr{L}$ is the typical length scale; otherwise, Levy motion may make new solutions (even) jump outside of the design domain. The u and v parameters are obtained from the following equations.

$$u \; N(0, \sigma_u^2), \sigma_u = \left(\dfrac{\Gamma(1+\beta)\sin(\pi\beta/2)}{\beta\Gamma[(1+\beta)/2]2^{(\beta-1)/2}}\right) \quad (11)$$

$$v \; N(0, \sigma_v^2), \sigma_v = 1 \quad (12)$$

where $0 < \beta \leq 2$, and Γ is the gamma function defined as:

$$\Gamma(y) = \int z^{y-1}e^{-y}dt \quad (13)$$

2.2.2. LSMA-based decision tree kernel

In this study, the decision tree method (DT) is used as a kernel or objective function to assess each slime mould in each iteration. The advantages of using the DT method as a kernel function are as follows; it is a robust method and requires less time computation for training, and requires a small set of training data. The following kernel function formula is used to assign fitness value to each SM in the search space through the optimization process:

$$Fitness_{val} = (1-\delta)\cdot(1 - DT_{ACC}) + \delta\cdot\dfrac{S_{attr}}{(L_{attr} - 1)} \quad (14)$$

where δ is a balance factor (set to $\delta = 0.01$, after different trials), DT_{ACC} is the DT accuracy, S_{attr} is the summation of selected features, and L_{attr} is the length of selected features. The goodness of each subset of features represented by SM position in the feature space is assessed by kernel-based DT function.

2.3. Adaptive fuzzy C-Means (AFCM)

The segmentation of medical images is an essential task that permits to perform posterior analysis of the objects. Then it is crucial to have a robust technique that permits handling the challenges of medical images. Based on this fact, the Fuzzy C-Means (FCM) is considered one of the most popular approaches for image clustering [26–31]. The FCM is regarded as a part of the unsupervised clustering techniques, and it has been widely used to solve complex problems. However, it is not a perfect method, and its drawbacks are the computational effort that depends on the number of clusters and the accuracy that is affected by the noise of the datasets.

The FCM process starts by considering that object O is a set of p pixels, and C is the set of c centroids in an n-dimensional feature space. To classify each pixel, the algorithm uses the following objective function iteratively:

$$J = \sum_{j=1}^{n} \sum_{i=1}^{c} \mu_{ij}^{m} |O_j - C_i|^2 \quad (15)$$

Algorithm 1: Steps of SMA algorithm.

1: Initialize parameters N_{agent}, Max_t.

(*continued on next page*)

(continued)

Algorithm 1: Steps of SMA algorithm.

2: Initialize slime mould positions X_i.
3: *While* ($t \leq Max_t$)
4: Calculate the fitness of all SM;
5:     *Update best Fitness*, X_b
6: Calculate W by Eq. (5);
7: *For each agent*$_i$
8:     *Update p, vb, vc.*
9:     *Update positions by* Eq.(7).
10: *End For*
11:   $t = t + 1$;
12: *End While*
13: Return **Optimal solution X_b.**

where m is a weighted index parameter $m \in [1, \infty]$, C_i is the ith cluster centers, and μ_{ij} is the fuzzy membership which can be calculated as follows:

$$\mu_{ij} = 1 \Big/ \sum_{k=1}^{c} \left(\frac{d_{ij}}{d_{kj}}\right)^{2/m-1} \qquad (16)$$

where d_{ij} is the Euclidian distance. The objective function is minimized during the process of clustering, the pixels close to cluster centroid have been assigned high membership values, and these membership values are updated in each iteration. The FCM stops when the criteria are satisfied (the centroids of the previous and current iteration are identical).

In medical images and especially in chest X-ray images for COVID-19 infection detection, the implementing of the algorithms applied during the life pandemic should be accurate and fast. Nevertheless,

conventional FCM may not have enough convergence speed, especially in emergency conditions. The FCM assigns membership values to every pixel and iteratively updating the cluster centers. Updating the membership matrix is, therefore, a time-consuming procedure. Thus, the adaptive-FCM (AFCM) is proposed using the histogram of the image intensities (maximum (I_{max}) and minimum (I_{min})) through the clustering process instead of the raw image data to reduce time computation in the standard FCM. The steps of the adaptive FCM are shown in Algorithm 2.

Algorithm 2: Adaptive fuzzy c-means (AFCM)

Input: X-ray image (I).
Output: Labeled image.
1: Compute image histogram (I_{hist}).
2: Compute range of intensity (I_{min}, I_{max}).
3: Initialize cluster centroids.
4: Update fuzzy memberships and centroids.
5: *While (Pre centroid $<>$ Cur centroid)*
6: *For each Pixel (P) in I_{hist}*
7: Compute Euclidian distance.
8: Compute fuzzy memberships for each P in I_{hist}.
9: *End For*
10: *End While*
11: Update centroids.
12: Defuzzify and create image label.

3. The proposed AFCM-LSMA model

In this section, the proposed new model is presented based on adaptive-FCM and Lévy-SMA to analyze and diagnose patients with COVID-19 from CXR scans using a set of real data. The proposed optimization model consists of five phases: preprocessing, segmentation,
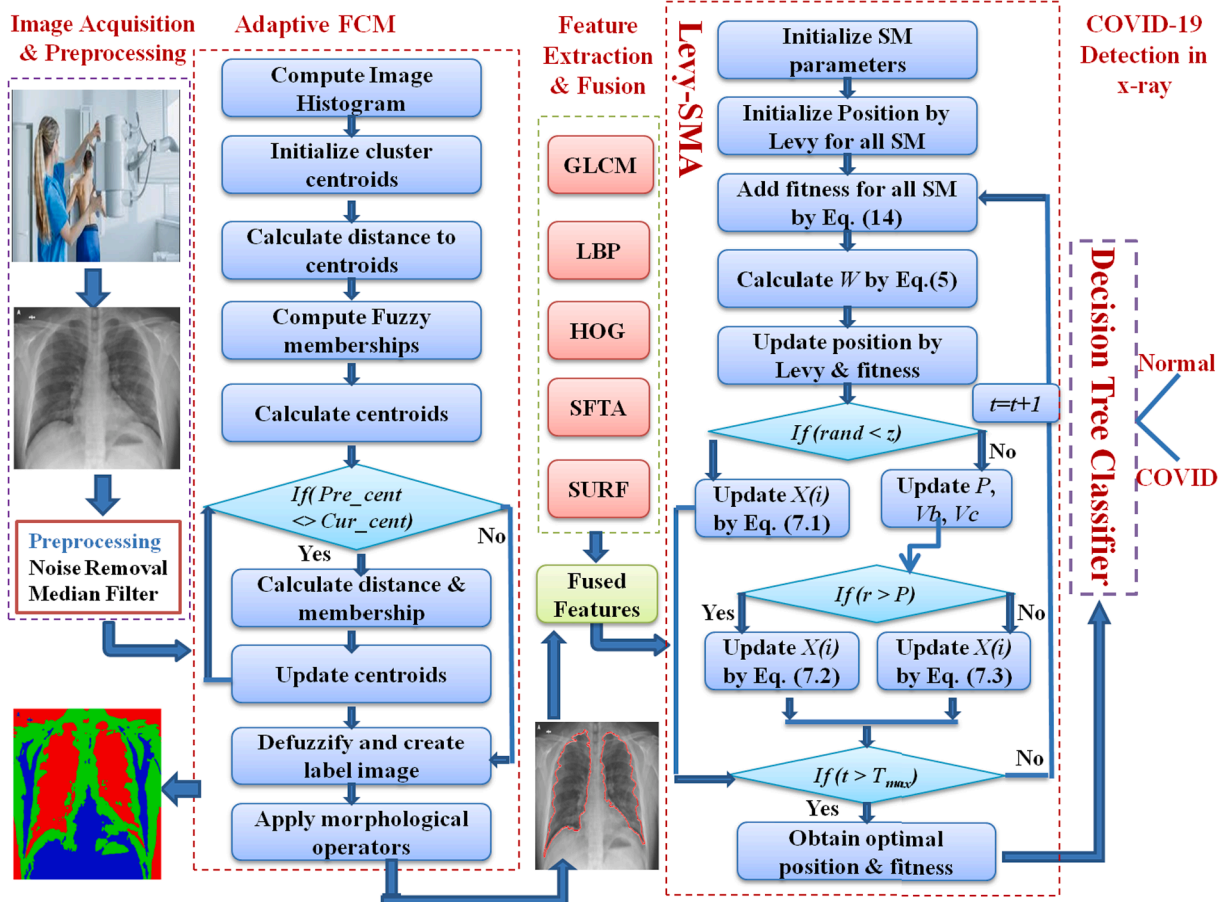

Fig. 3. Pipeline of the proposed AFCM-LSMA model for COVID-19 detection in chest X-ray images.

feature extraction, feature fusion and selection, and identification with decision making. The following is a detailed description of each phase, with the steps involved and the characteristics for each phase. Fig. 3 shows the pipeline of the proposed AFCM-LSMA model for infected COVID-19 identification based on CXR images.

- **Preprocessing phase**. In this phase, X-ray images are converted into a gray-scale levels and resized to reduce computational time. The adaptive noise removal (ANR) filter is used to remove noise and to reflect the true intensities of the images. The ANR uses a pixel-wise adaptive wiener method based on statistics estimated from a local neighborhood of each pixel. Then, the median filter is applied with median size 5-by-5 neighborhood to the input CXR image.

- **Segmentation phase.** The pulmonary regions are segmented in this phase from CXR images. Here the adaptive-FCM is proposed to automatic cluster images and segment pulmonary regions from the CXR images, and morphological operators are used to refine segmentation results. The intensities histogram of the CXR image (I_{min}, I_{max}) is utilized during the clustering process instead of raw image data. Arguably, the AFCM does not depend on the whole CXR image, and it depends on the frequencies of the CXR images. The AFCM method is less sensitive to noise, it reduces the computational time of clustering and increases the performance of conventional FCM.

- **Feature extraction phase**. In this phase, the high-level features with different scales are extracted from the segmented pulmonary regions using five different feature selection methods GLCM [37], HOG [38], LBP [37], SFTA [39], and SURF [40]. As the extracted features are the base for classifying the COVID-19, the classification techniques also resulted in low classification accuracy. There is a consensus that no single feature has a perfect performance because every feature has its limitations. To resolve these issues, features are fused to increase the rate of classification accuracy.

- **Feature fusion and selection phase**. After feature extraction of each candidate region by the five feature extraction methods, these feature vectors of the same X-ray pulmonary regions are concatenated to form higher dimensional fusion features. This can compensate for the inadequacy of a single method in the feature extraction. However, there always exist irrelevant, some correlation, and information redundancy between these features and higher dimensional features lead to higher computational complexity. Therefore, the LSMA is adopted to determine the significant features from the high dimensional feature fusion matrix. In this sense, a subset of features can be regarded as a point in a large feature space. In the search space, the SMA population is stochastically initialized and moves randomly to change their positions; this is called continuous space. Feature selection issues are restricted to the values of binary space [0,1]; thus, continuous features are converted into their corresponding binary solutions. A 0 or 1 is represented for each value in the feature vector. A 1 means the corresponding feature is selected, while the value set to 0 means the corresponding feature is not selected. In the search space, the fitness value is given to each SM and assessed in each iteration. The fitness of each SM is initialized using kernel-based DT function as seen in Eq. (14). This kernel function is used as a part of the optimizer to validate the significant features. Besides, to control the exploitation and exploitation phases in SMA, Lévy motion (non- Gaussian distribution) is embedded in SMA to generate a fraction of solutions that are apart from existing solutions and far enough from the current solution. Such far help the SMA optimizer to escape from local optima and finds global solutions, avoids stagnation, increases the efficiency in examining large search areas, and improves the global search capability.

- **Diagnosis and decision-making phase**. In this phase, a simple decision tree method is used for the identification of infected COVID-19 from CXR images after the feature fusion and selection phase. The advantages of the DT-based classification are self-explanatory logic flow, richness in representing discrete-value classifiers, less time

computation, ability to handle small datasets, and ability to handle missing data values and error.

4. Experimental results and discussion

The proposed new optimization model for COVID-19 detection from CXR images is implemented and tested on an Intel® CoreTM i7-2670QM 2.5 GHz processor with 16 GB RAM using MATLAB (R2016a, The MathWorks, Inc.). To evaluate the proposed AFCM-LSMA model, numerous measures are utilized to compare different methods and to assess the feature selection and classification process for COVID-19 diagnosis. These measures are best fitness score (*BFS*), worst fitness score (*WFS*), standard deviation (S_{td}), average attribute selection (*AAS*), accuracy (*ACC*), computational time (*time*), root mean square error (*RMSE*), false-positive rate (*FPR*), sensitivity, specificity, precision, *F1_score*, kappa coefficient (*Kappa*), Matthews correlation coefficient (*MCC*), informedness (*Informed*) and markedness (*Marked*) [15,16].

4.1. Parameters setting

LSMA has a set of parameters that need to be initialized before the optimization process. Table 1 shows the parameters setting used in the experiments for all the competitive algorithms (Ant Lion Optimizer (ALO) [41], Grey Wolf Optimizer (GWO) [16], Whale Optimization Algorithm (WOA) [17], Bat algorithm (BAT) [42]). These parameters include the number of search agents (N_{Agents}), upper and lower limits (U and L), the maximum number of iterations ($Iter_{Max}$), space dimension (S_d), and binary domain search (B_{SD}).

4.2. Segmentation based-AFCM algorithm

The X-ray images obtained by the medical personal need to be processed before extract the essential information. Fig. 4 shows the output of different steps performed for the prepossessing and segmentation of the pulmonary region in the CXR images. In this figure, the CXR images (CXR_Imgs) 1 and 2 correspond to the normal patients; meanwhile, the

Table 1
Parameters setting used in the experiments.

Algo.	Parameters	Init.	Description
ALO	T_{Max}	50	Total no. of iterations
	N_{Agents}	5	No. of ants search agents
	S_D	672	Space Dimension
	B_{SD}	[01]	Binary domain search
	[U L]	[10]	Upper and Lower bound
WOA	T_{Max}	50	Total no. of iterations
	N_{Agents}	5	No. of whales search agents
	S_D	672	Space Dimension
	B_{SD}	[01]	Binary domain search
	[U L]	[10]	Upper and Lower bound
GWO	T_{Max}	50	Total no. of iterations
	N_{Agents}	5	No. of Wolves search agents
	S_D	672	Space Dimension
	B_{SD}	[01]	Binary domain search
	[U L]	[10]	Upper and Lower bound
BAT	T_{Max}	50	Total no. of iterations
	N_{Agents}	5	No. of bats search agents
	S_D	672	Space Dimension
	B_{SD}	[01]	Binary domain search
	[U L]	[10]	Upper and Lower bound
SMA	T_{Max}	50	Total no. of iterations
	N_{Agents}	5	No. of slim search agents
	S_D	672	Space Dimension
	B_{SD}	[01]	Binary domain search
	[U L]	[10]	Upper and Lower bound
	δ	0.01	DT balance factor
	Z	0.03	Explor. and exploit. factor
FCM	q	2	Fuzzifier Index
	c	3	No. of clusters

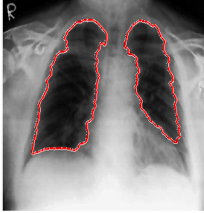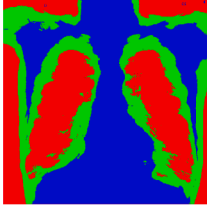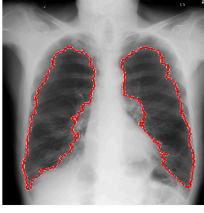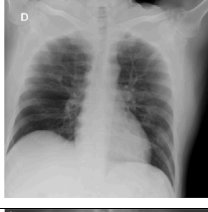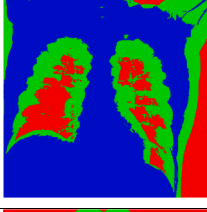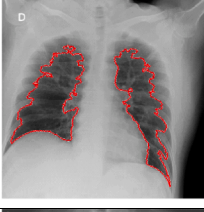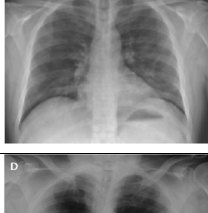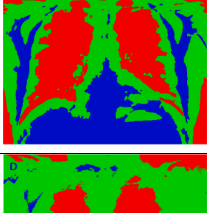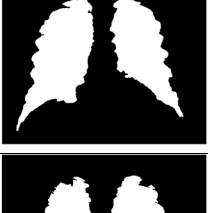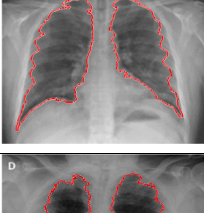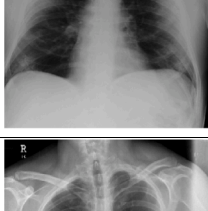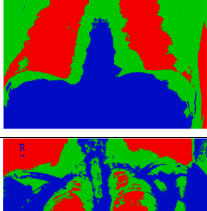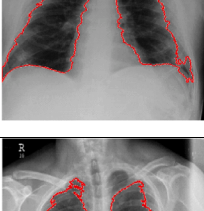| Img	Filtering	Segmentation AFCM	Morphological Operat.	Segmented lung
1				
2				
3				
4				
5				
6				

Fig. 4. Segmentation results of the proposed Adaptive FCM for different normal and infected COVID-19 X-ray patients. CXR_Img 1 and CXR_Img 2 correspond to normal patient's X-ray, and the remaining are of the X-ray of infected COVID-19 patients.

rest are for COVID-19 infected patients. The CXR images are then firstly filtered to remove noise by adaptive wiener filter, and then the median filter is applied to smooth image with median value a 5-by-5 neighborhood around the corresponding pixel in the input CXR image. Fig. 4 (a) shows the results of the preprocessing steps in the filtering column. Consequently, images are passed to adaptive-FCM for clustering and segmentation. The FCM clustering algorithm is adapted to be suitable for the problem of COVID-19 detection, as shown in Fig. 4 (b). Before getting the final output, morphological operations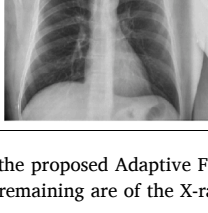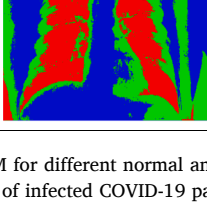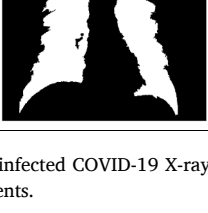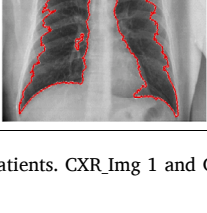 are applied to make the segmented lungs more solid objects as shown in Fig. 4 (c). The segmented lungs are then used in the feature extraction phase as shown in Fig. 4(d).

4.3. Feature extraction

After the segmentation results are generated, the pulmonary regions

identified are used as an input to the feature extraction process. The idea of this task is to obtain the information that describes infected and healthy tissue. Five different feature extraction methods are used GLCM, HOG, LBP, SFTA, and SURF to extract features from the segmented pulmonary regions. They are experimentally selected considering the information provided. Thus, features are extracted using different methods for different scales of features to increase the rate of classification performance. GLCM is used to extract the second-order statistical texture features and to provide spatial relationships of pixels in the segmented image. It provides vectors with size 68 feature values computed from the following 17 formula (energy, entropy, homogeneity, contrast, dissimilarity, angular second moment, correlation, variance, maximum probability, cluster tendency, cluster shade, cluster prominence, sum-average, sum variance, sum entropy, entropy difference, difference-variance) with four orientations and one distance. LBP is an efficient texture feature uses to labels the pixels of an image by

thresholding the neighborhood of each pixel. Due to its discriminative power and computational simplicity, LBP has become a popular method in various applications. LBP is used to provide vectors with size 4 texture feature values from (mean, standard deviation, skewness, and kurtosis). HOG uses for the purpose of object detection. This method counts occurrences of gradient orientation in localized portions of an image. HOG is similar to that of edge orientation histograms, scale-invariant feature transform descriptors (SIFT), and shape contexts, but differs in that it is computed on a dense grid of uniformly spaced cells to improve accuracy. In this study, HOG is used to provide vectors with size 500 feature values of gradient features. SFTA method is used to decompose the segmented pulmonary CXR image into a set of binary images from which the fractal dimensions of the resulting regions are computed to describe texture patterns. SFTA uses to provide vectors with size 36 features. SURF method provides a local feature detector and descriptor to recognize objects. SURF uses to detect interest key-points based on the Hessian matrix. Simplify the operation and helps to reduce the computational cost by applying appropriate filters to the integral image. Haar wavelet responses in *x* and *y* directions are computed to determine the orientation. Based on the integral image and Hessian matrix, robust keypoint descriptors are detected by using the SURF algorithm. In this study, SURF provides vectors with size 64 feature values. All this information then is fused and stored in a high dimensional matrix for posterior steps.

4.4. Feature fusion and selection

Feature fusion of the extracted features helps to learn image features fully for the description of their rich internal information, to obtain a compact representation of integrated features, and to form a matrix with high dimensional features. However, to reduce redundant data, remove irrelevant, and obtain optimal features, the enhanced LSMA algorithm is used as a feature selection method to identify the optimal and most representative features that describe the instances of the dataset generated in the previous phase. The enhanced LSMA is then firstly compared with the conventional SMA to verify its performance over this task. Fig. 5 shows that the convergence curve using the decision tree as an objective function. In the plot, it is shown that the optimal fitness value looked for by SMA varies with iterations. The convergence curve shows the behavior of the algorithm and how the processes of exploration and exploitation are applied. Besides, the speed of convergence of the LSMA is superior to find the optimal values.

Table 2 presents an analysis of the optimization results obtained by the LSMA and the SMA for the feature extraction. From this table, it is possible to analyze that the LSMA provides better values in terms of the

Table 2
Results of the proposed LSMA compared with classical SMA in terms of best and worst fitness, μ, *Std*, time, and *ACC*.

Algor.	μ	*Std*	*WFS*	*BFS*	*Time*	*ACC*
SMA	0.0325	6.5388e−04	0.0334	0.0319	56.0668	0.9395
LSMA	0.0265	0.0032	0.0334	0.0247	42.2139	0.9586

objective function. Besides, the worst value after 35 independent runs are similar for both algorithms; however, the best value of the runs is for the LSMA. The computational time is also lower for the LSMA, and the Accuracy (*ACC*) of the classification is also better for LSMA.

Regarding the different metrics used in classification and feature selection, Table 3 presents a comparative analysis between the SMA and the LSMA based on different measures calculated. As we can see, the proposed model based on Lévy motion has good performance and is superior in most of the metrics as in *ACC, RSME, time, error, precision*, the average number of attribute selection (*AAS*), false-positive error (*FPR*). Moreover, *F1-score* is 0.9767 that represents a perfect precision and recall even if the data is unbalanced, and *Kappa* is 0.791 that represents a good agreement based on *Kappa* coefficient criteria where $0.60 < k > 0.80$, where *Informedness* is 0.801 that measures how informed the model is about positives and negatives predictions. More details about SMA and LSMA can be seen in Table 3.

Since the proposed LSMA is a modified version of the SMA using different distributions for random variables, then it is necessary to compare it with another kind of distributions. In this sense, six chaotic maps are considered, namely Chebyshev, Circle, Logistic, Sine, Singer, and Tent. Fig. 6 shows the convergence curve for SMA with different chaotic maps and Levy motion distributions. From this plot, we can see that Lévy motion is the highest convergence (in around 15 iterations) to the optimal solution compared with other chaotic maps. Moreover, from Table 4 it is possible to analyze the results generated by the fitness and the accuracy of the classification using different chaotic maps and the LSMA (Lévy motion). In terms of fitness, the version based on Lévy motion provides the best mean value after 35 independent runs. In the same way, the LSMA is better for *ACC* and computational time. The worst mean fitness is for the Singer and Chebyshev maps, but the Singer map is the best for the S_{td}. Considering the results, we can prove that the LSMA is a competitive option that provides more accurate detection of COVID-19 cases in X-ray images and less computational time. More details about SMA versions with Lévy and different chaotic maps can be seen in Table 4.

Table 5 also shows a comparative study of the feature selection and classification tasks by using different evaluation criteria. From such a table, we can see that the classification accuracy is better for the Lévy-SMA *ACC* (≈ 0.96), followed by SMA integrated with the Sine map (≈ 0.94), and the worst for the Singer map (≈ 0.93). The *RMSE* is also better for the Lévy-SMA (≈ 0.23), followed by Sine-LSMA (≈ 0.24) and

Fig. 5. Convergence curve of the proposed LSMA compared with conventional SMA algorithm.

Table 3
Results of the proposed LSMA compared with classical SMA using different measurement criteria.

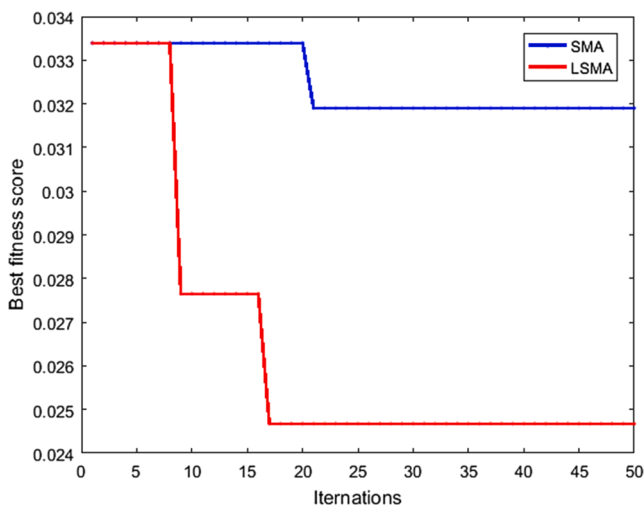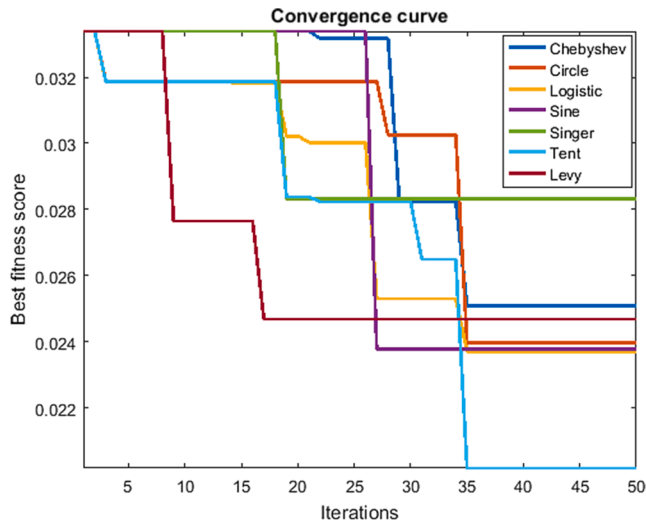| Measure	SMA	LSMA
ACC	0.940	0.959
RMSE	0.236	0.233
Time	56.067	42.214
AAS	0.353	0.103
Sensitivity	0.998	0.975
Specificity	0.484	0.826
Precision	0.946	0.979
FPR	0.516	0.174
F1_score	0.971	0.977
MCC	0.660	0.791
Kappa	0.618	0.791
Informed.	0.482	0.801
Marked.	0.904	0.781

Fig. 6. Convergence curve for SMA with different chaotic maps and Lévy distributions.

Table 4
Results of the proposed SMA algorithm modified by different chaotic maps and Lévy motion distribution in terms of best and worst fitness, μ, *Std*, time, and *ACC*.

Version	μ	Std	WFS	BFS	Time/s	ACC
Chebysh.	0.030	0.004	0.033	0.02	77.33	0.936
Circle	0.029	0.004	0.033	0.024	69.61	0.935
Logistic	0.028	0.004	0.033	0.024	136.02	0.936
Sine	0.029	0.005	0.033	0.024	78.98	0.940
Singer	0.030	0.003	0.033	0.028	69.06	0.934
Tent	0.027	0.005	0.033	0.020	68.87	0.935
Lévy	0.027	0.003	0.033	0.025	42.21	0.959

also worst for Singer ($\approx$0.26). In terms of the computational time, the best is SMA based-Lévy ($\approx$0.42 s), but the most time-consuming is the Logistic map ($\approx$0.136 s). The lower error is also for the Lévy version and the worst for the Singer map. The precision of the LSMA is also superior for the classification task. Besides, the minimum average of the attribute selection is better for LSMA with high *ACC* accuracy and less *FPR* error. The *MCC* is also superior for the LSMA, which takes into consideration true, false positives, and negatives and is generally considered a balanced measure that can be used even if the classes with imbalance size. *Kappa* is also superior, which represents a good agreement. More details about measurement criteria for SMA versions with Lévy and chaotic maps can be seen in Table 5. From these results, we can confirm that the proposed SMA-based Lévy motion distribution is better than other chaotic distribution.

4.5. Comparison between different meta-heuristic optimization methods

In this subsection, the performance of the proposed AFCM-LSMA is analyzed in comparison to other recent meta-heuristic optimization methods such as ALO, Singer version of ALO, WOA, Chebyshev version of WOA, Circle version of WOA, Chebyshev version of GWO, Gauss version of GWO, BAT and the standard SMA. Those optimization algorithms are selected due to the high performance provided in global optimization and real problems. In comparative experiments, all algorithms are carried out under the same conditions for achieving fairness.

Fig. 7 presents a graphical comparison between all the selected meta-heuristic optimization methods along with the 50 iterations. From this figure, the LSMA algorithm converges in around 15 iterations, and the worst obtains by the WOA. In the plot of the LSMA, it is possible to see the influence of Lévy distribution to change between exploration and exploitation for finding the optimal solution.

Regarding the results of classification and feature selection, Table 6 presents the results based on different metrics. The *ACC* of the classification of COVID-19 patients is superior for the LSMA ($\approx$0.96), followed by the standard SMA with *ACC* ($\approx$0.96) and the worst for the WOA ($\approx$0.90), but the accuracy of WOA is increased when the Sine chaotic map is integrated with WOA provides *ACC* ($\approx$0.93). The best *RMSE* is also for the LSMA ($\approx$0.23), followed by standard SMA with *RMSE* ($\approx$0.24) and the higher for WOA ($\approx$0.32), and also the *RMSE* is improved when WOA is integrated with Sine chaotic map with *RMSE* ($\approx$0.27). In addition, the less computational time is archived from the proposed LSMA with ($\approx$42 s), followed by SMA ($\approx$56 s) and the worst for the Chebyshev map of WOA ($\approx$160 s). This situation also occurs for *precision*, *FPR*, *F1_score*, *MCC*, *kappa*, the *error*, *Informed*, and the average number of selected attributes (*AAS*). More details about other meta-heuristic algorithms can be seen in Table 6. From these results, we can also confirm the robustness and the superiority of the proposed AFCM-LSMA algorithm against different meta-heuristics and swarm intelligence optimization algorithms for COVID-19 detection in chest X-ray images.

4.6. Comparison between different machine learning (ML) methods

This section provides the comparison results between the proposed AFCM-LSMA method and other ML methods for COVID-19 detection in chest X-ray images, including K-Nearest Neighbor (KNN), Naïve Bayes (NB), Linear Discriminate Analysis (LDA) with linear and quadratic kernels, Support Vector Machine (SVM) with Radial basis function (RBF) and Gaussian kernels, and Random Forest (RF). Moreover, the proposed method is compared with different artificial neural network methods, including Back-Propagation Neural Network (BP-NN), Generalized Regression Neural Network (GRNN), and Probabilistic Neural Network (PNN).

The comparison results are shown in Table 7 and Fig. 8. It can be seen that the proposed AFCM-LSMA method can achieve the highest accuracy

Table 5
Results of the proposed SMA algorithm modified by other six chaotic maps and Lévy motion distribution using different measurement criteria.

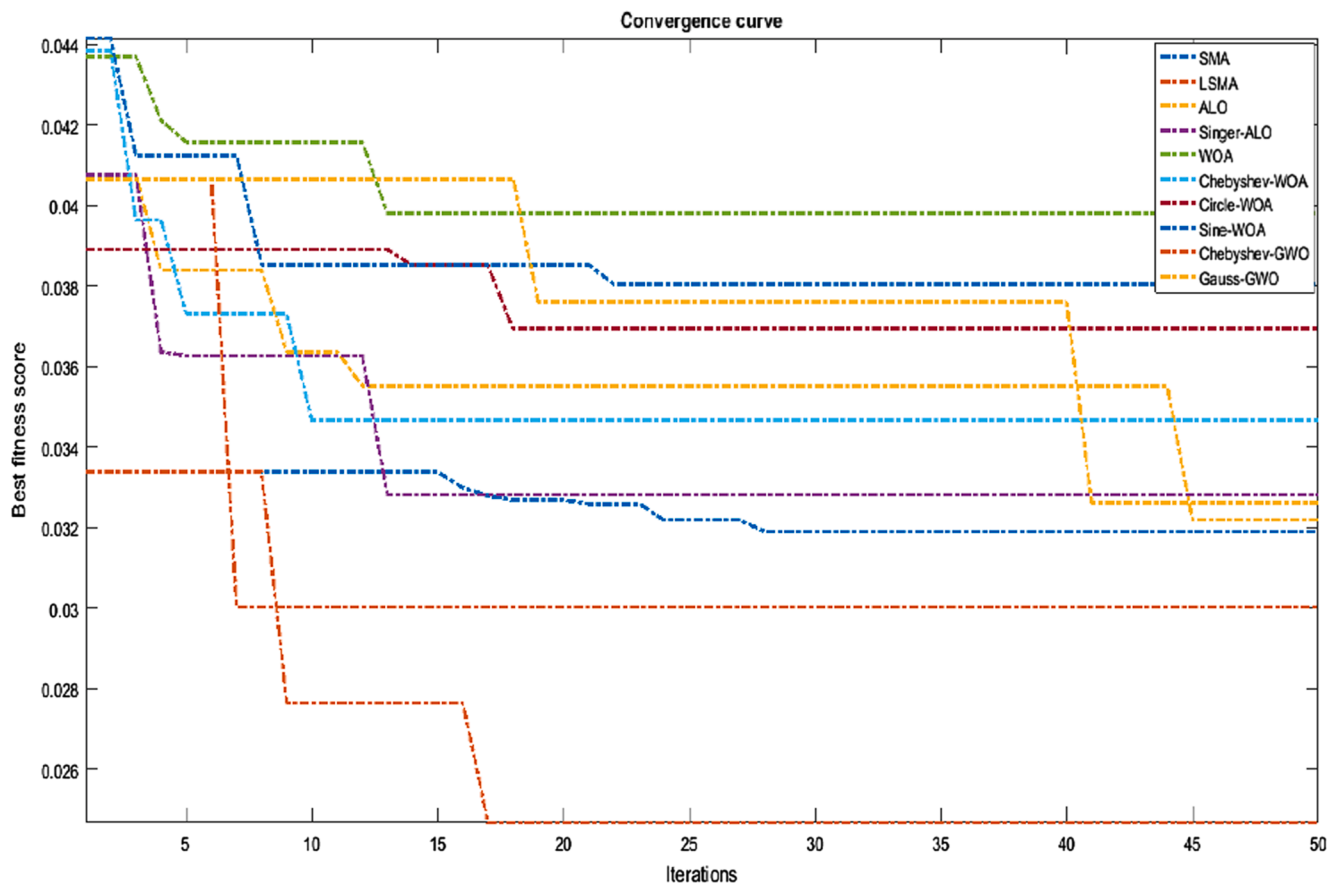| Measure	Cheby.	Circle	Logist.	Sine	Singer	Tent	Lévy
ACC	0.9363	0.9352	0.9363	0.9395	0.9342	0.9352	0.9586
RMSE	0.2524	0.2545	0.2524	0.2460	0.2565	0.2545	0.2327
AAS	0.4580	0.5059	0.4791	0.4866	0.4672	0.4405	0.1026
Error	0.0637	0.0648	0.0637	0.0605	0.0658	0.0648	0.0414
Sensitiv.	0.9918	0.9953	0.9941	0.9929	0.9941	0.9906	0.9750
Specific.	0.4301	0.3871	0.4086	0.4516	0.3871	0.4301	0.8261
Precis.	0.9408	0.9368	0.9388	0.9430	0.9367	0.9407	0.9785
FPR	0.5699	0.6129	0.5914	0.5484	0.6129	0.5699	0.1739
F1_scor	0.9656	0.9652	0.9657	0.9673	0.9646	0.9650	0.9767
MCC	0.578	0.5657	0.5755	0.6030	0.5573	0.5706	0.7911
Kappa	0.541	0.5124	0.5294	0.5666	0.5076	0.5362	0.7910
Inform.	0.4219	0.3824	0.4027	0.4445	0.3812	0.4207	0.8010
Marked.	0.7918	0.8368	0.8225	0.8180	0.8148	0.7740	0.7813

Fig. 7. Convergence curve of different swarm intelligence algorithms compared with the proposed LSMA algorithm.

Table 6
Results of the proposed LSMA compared with the counterpart meta-heuristic algorithms.

Measures	ALO	Singer-ALO	WOA	Cheby-WOA	Circle-WOA	Sine-WOA	Cheby-GWO	Gauss-GWO	BAT	SMA	LSMA
ACC	0.937	0.935	0.895	0.922	0.917	0.927	0.922	0.924	0.920	0.940	0.959
RMSE	0.250	0.255	0.324	0.279	0.288	0.271	0.279	0.277	0.282	0.236	0.233
Time/s	112.51	74.974	158.09	160.24	156.59	159.28	92.48	157.83	99.31	56.07	42.21
AAS	0.595	0.268	0.936	0.946	0.964	0.970	0.487	0.952	0.504	0.353	0.103
Error	0.063	0.065	0.105	0.078	0.083	0.073	0.078	0.078	0.076	0.053	0.041
Prec.	0.935	0.938	0.892	0.923	0.913	0.929	0.9198	0.921	0.920	0.946	0.979
FPR	0.634	0.602	0.795	0.723	0.650	0.661	0.742	0.727	0.742	0.516	0.174
F1_scor	0.966	0.965	0.943	0.958	0.955	0.961	0.958	0.959	0.957	0.971	0.977
MCC	0.585	0.567	0.427	0.474	0.565	0.519	0.487	0.501	0.470	0.660	0.791
Kappa	0.510	0.519	0.309	0.394	0.485	0.458	0.383	0.402	0.377	0.618	0.791
Inform.	0.366	0.392	0.205	0.273	0.350	0.333	0.258	0.273	0.256	0.482	0.801
Marked.	0.935	0.819	0.892	0.823	0.913	0.809	0.919	0.921	0.864	0.904	0.781

Table 7
Comparison results between the proposed method and different ML methods under different evaluation criteria.

| Meth.	*ACC*	*Err*	*Sens.*	*Spec.*	*Precis*	*FPR*	*F1*	*MCC*	*Kappa*	*Inform*	*Marked*	*Time*
KNN	0.904	0.096	0.974	0.349	0.923	0.651	0.948	0.422	0.401	0.323	0.551	1.023
NB	0.889	0.112	**1.000**	0.000	0.889	1.00	0.941	–	0.000	0.000	0.000	4.438
LDA-L	0.913	0.087	0.932	0.762	0.969	0.238	0.950	0.620	0.613	0.694	0.554	4.803
LDA-Q.	0.876	0.124	0.904	0.651	0.954	0.349	0.928	0.480	0.470	0.555	0.415	4.056
SVM-RBF	0.906	0.094	0.982	0.302	0.918	0.698	0.949	0.411	0.375	0.284	0.597	1.141
SVM-G.	0.897	0.103	0.980	0.238	0.911	0.762	0.944	0.334	0.296	0.218	0.511	0.862
RF	0.927	0.073	0.962	0.651	0.956	0.349	0.95	0.626	0.626	0.613	0.640	**0.194**
GRNN	0.890	0.110	0.940	0.508	0.936	0.492	0.938	0.454	0.454	0.448	0.460	18.52
PNN	0.892	0.108	0.892	**1.000**	**1.000**	**0.000**	0.943	0.168	0.055	**0.892**	0.032	23.93
BP-NN	0.926	0.074	0.924	0.957	0.998	0.044	0.960	0.553	0.481	0.881	0.347	1.277
LSMA	**0.959**	**0.041**	0.975	0.826	0.979	0.174	**0.977**	**0.791**	**0.791**	0.801	**0.781**	42.21
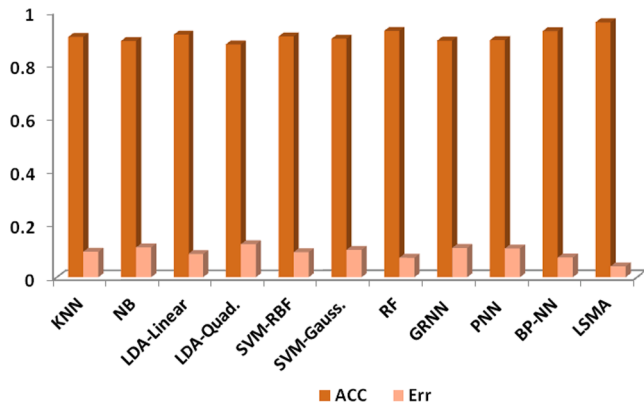
Fig. 8. Graphical representation for the proposed method and different ML methods.

Fig. 9. Graphical representation for the proposed method and different DL methods with different hidden layers.

($\approx$0.959), while its sensitivity ($\approx$0.975), specificity ($\approx$0.826), precision ($\approx$0.979), FPR ($\approx$0.174), markedness ($\approx$0.781), and F1-score ($\approx$0.977) were also the best or close to the best results. Followed by the results achieved by PNN with accuracy ($\approx$0.892), sensitivity ($\approx$0.892), specificity ($\approx$1.00), precision ($\approx$1.00), F1-score ($\approx$0.943), and informedness ($\approx$0.892). More details about other ML methods can be seen in Table 7. In conclusion, the proposed AFCM-LSMA method is superior to conventional ML methods.

Recently, deep learning (DL) has become a popular method with different architectures that can classify medical data with good accuracy. In this study, three different deep learning methods with different hidden layers are provided, including Feed Forward Neural Network (FFNN), Cascade Forward Neural Network (CFNN), and Recurrent Neural Network (RNN). These DL methods are compared with the proposed AFCM-LSMA method for COVID-19 detection in chest X-ray images. Table 8 and Fig. 9 show the comparison results between the proposed method and the DL methods under different evaluation criteria. As we can see, the proposed method achieves good results with less computational time, meanwhile, the results of the RNN method achieve the same or near results with the proposed method, but it still has some deficiencies and shortcomings. For example, it is time-consuming and lacks transparency, and it has no proven guaranteed convergence. With an increased demand for real-time data analysis, the time to quickly retrain DL methods to understand new COVID-19 cases may not be sufficient to keep up with the pace of data inflow. From these results, we can confirm the robustness and the superiority of the proposed method against different classical machine learning and deep learning methods for COVID-19 detection in chest X-ray images.

The main limitation associated with our study is the publicly available dataset size. The chest X-ray images used in this study comprise information of 1124 patients (403 with COVID-19 and 721 normal patients). This data is trained to classify the input CXR images into one of two classes (COVID-19 infected or normal patients). There are imbalanced data and bias to normal patients. Therefore, data can be balanced

by withdrawing some features, or a generative adversarial neural network (GAN) can be used to generate synthetic data for imbalanced data problems. In addition, the execution of the proposed deep learning methods can be improved with a larger COVID-19 dataset. Moreover, the overall results are restricted only to the COVID-19 X-ray image.

5. Conclusion and future work

The main aim of the proposed work is to develop an image-assisted analysis model based on chest X-ray to evaluate and assess the detection of COVID-19. The X-ray scan is recognized as an important tool for COVID-19 assessment. Unfortunately, a corona-virus vaccine is expected to take at least 18 months if it works at all. Moreover, COVID-19 pandemics may mutate into a more aggressive form, according to World Health Organization (WHO). Therefore, this paper proposed a new COVID-19 detection model based on adaptive fuzzy c-mean clustering algorithm and Lévy slime mould algorithm for chest X-ray images. In the clustering phase, the intensity of the image histogram is computed instead of the raw image to reduce time and amount of computations and decrease the sensitivity of noise. The slime mould optimization algorithm is integrated with Lévy motion to select the significant features from the high dimensional feature fusion matrix. SMA uses the weights to mimic the positive and negative feedback of the bio-oscillator in order to produce a specific thickness of the feeding vein network during the foraging to the food source. Lévy motion distribution is used as a permutation for performing a local search, escaping from local minima, and reaching the optimal solution in fewer iterations with high convergence speed. The performance of the proposed AFCM-LSMA model has been validated using different measurements on CXR images and compared with different state-of-art meta-heuristic and machine learning methods. Moreover, the proposed method is compared with different DL methods to ensure stability and efficiency. The experimental results demonstrate the superiority of the proposed model, and it can be useful for the clinical practitioner for early identification of COVID-19 infected patient. In future research, we will increase the dataset of COVID-19

Table 8
Comparison results between the proposed method and deep learning approachess with different hidden layers (*HLs*) under different evaluation criteria.

Meth.	HLs	ACC	Err	Sens.	Specific	Prec.	FPR	F1_scor	MCC	Kappa	Inform	Marked
FFNN	**5**	0.889	0.112	0.889	–	**1.00**	–	0.941	–	0.00	–	0.00
	10	0.927	0.073	0.926	0.958	0.998	0.042	0.961	0.567	0.498	0.884	0.363
	15	0.927	0.073	0.926	0.958	0.998	0.042	0.961	0.567	0.498	0.884	0.363
CFNN	**5**	0.939	0.060	0.937	**1.000**	**1.000**	**0.000**	0.967	0.657	0.603	**0.937**	0.460
	10	0.936	0.064	0.962	0.721	0.966	0.279	0.964	0.674	0.674	0.684	0.665
	15	0.936	0.064	0.940	0.886	0.992	0.114	0.965	0.632	0.601	0.825	0.484
RNN	**5**	0.912	0.089	0.931	0.659	0.972	0.342	0.951	0.486	0.473	0.590	0.401
	10	**0.958**	0.043	0.969	0.855	0.984	0.146	**0.976**	0.775	0.773	0.823	0.730
	15	0.889	0.116	0.889	–	**1.00**	–	0.941	–	0.00	–	0.000
LSMA	–	**0.959**	**0.041**	**0.975**	0.826	0.979	0.174	**0.977**	**0.791**	**0.791**	0.801	**0.781**

infected patients, and more theoretical analysis will be conducted. The proposed model will use to train and classify other types of diseases (such as; bacterial pneumonia and viral pneumonia). Moreover, the proposed model will apply to different medical images for COVID-19 such as (CT and MRI scans).

Declaration of Competing Interest

The authors declare that they have no known competing financial interests or personal relationships that could have appeared to influence the work reported in this paper.

Compliance with Ethical Standards

Declaration of Competing Interest. The authors declare that they have no known competing financial interests or personal relationships that could have appeared to influence the work reported in this paper.

Ethical approval. This article does not contain any information with human participants or animals performed by any of the authors.

References

[1] Y.R. Guo, Q.D. Cao, Z.S. Hong, Y.Y. Tan, S.D. Chen, H.J. Jin, Y. Yan, The origin, transmission and clinical therapies on coronavirus disease 2019 (COVID-19) outbreak–an update on the status, Mil. Med. Res. 7 (1) (2020) 1–10.

[2] World Health Organization. Considerations for quarantine of individuals in the context of containment for coronavirus disease (COVID-19): interim guidance, 19 March 2020 (No. WHO/2019-nCoV/IHR_Quarantine/2020.2), 2020.

[3] I.D. Apostolopoulos, T.A. Mpesiana, Covid-19: automatic detection from X-ray images utilizing transfer learning with convolutional neural networks, Phys. Eng. Sci. Med. 1 (2020) 1–8, https://doi.org/10.1007/s13246-020-00865-4.

[4] M. Ienca, E. Vayena, On the responsible use of digital data to tackle the COVID-19 pandemic, Nat. Med. 26 (4) (2020) 463–464.

[5] G.S. Randhawa, M.P. Soltysiak, H. El Roz, C.P. de Souza, K.A. Hill, L. Kari, Machine learning using intrinsic genomic signatures for rapid classification of novel pathogens: COVID-19 case study, PLoS ONE 15 (4) (2020) e0232391.

[6] L. Li, L. Qin, Z. Xu, Y. Yin, X. Wang, B. Kong, K. Cao, Artificial intelligence distinguishes COVID-19 from community acquired pneumonia on chest CT, Radiology 200905 (2020).

[7] A.S. Al-Waisy, S. Al-Fahdawi, M.A. Mohammed, K.H. Abdulkareem, S.A. Mostafa, M.S. Maashi, B. Garcia-Zapirain, COVID-CheXNet: hybrid deep learning framework for identifying COVID-19 virus in chest X-rays images, Soft. Comput. (2020) 1–16.

[8] A.S. Al-Waisy, M.A. Mohammed, S. Al-Fahdawi, M.S. Maashi, B. Garcia-Zapirain, K.H. Abdulkareem, D.N. Le, COVID-deepnet: hybrid multimodal deep learning system for improving COVID-19 pneumonia detection in chest X-ray images, Cmc-Comput. Mater. Continua 67 (2) (2021) 2409–2429.

[9] M.A. Mohammed, K.H. Abdulkareem, B. Garcia-Zapirain, S.A. Mostafa, M. S. Maashi, A.S. Al-Waisy, D.N. Le, A comprehensive investigation of machine learning feature extraction and classification methods for automated diagnosis of covid-19 based on x-ray images, Comput. Mater. Continua 66 (3) (2020).

[10] M.A. Mohammed, K.H. Abdulkareem, A.S. Al-Waisy, S.A. Mostafa, S. Al-Fahdawi, A.M. Dinar, T. Díez, Benchmarking methodology for selection of optimal COVID-19 diagnostic model based on entropy and TOPSIS methods, IEEE Access 8 (2020) 99115–99131.

[11] K.H. Abdulkareem, M.A. Mohammed, A. Salim, M. Arif, O. Geman, D. Gupta, A. Khanna, Realizing an effective COVID-19 diagnosis system based on machine learning and IOT in smart hospital environment, IEEE Int. Things J. (2021).

[12] A.M. Ismael, A. Şengür, Deep learning approaches for COVID-19 detection based on chest X-ray images, Expert Syst. Appl. 164 (2021) 114054.

[13] S.R. Nayak, D.R. Nayak, U. Sinha, V. Arora, R.B. Pachori, Application of deep learning techniques for detection of COVID-19 cases using chest X-ray images: a comprehensive study, Biomed. Signal Process. Control 64 (2021) 102365.

[14] A. Gupta, S. Gupta, R. Katarya, Instacovnet-19: A deep learning classification model for the detection of covid-19 patients using chest x-ray, Appl. Soft Comput. 99 (2021) 106859.

[15] A.M. Anter, M. Ali, Feature selection strategy based on hybrid crow search optimization algorithm integrated with chaos theory and fuzzy c-means algorithm for medical diagnosis problems, Soft. Comput. 24 (3) (2020) 1565–1584.

[16] A.M. Anter, G. Huang, L. Li, L. Zhang, Z. Liang, Z. Zhang, A new type of fuzzy rule-based system with chaotic swarm intelligence for multi-classification of pain perception from fMRI, IEEE Trans. Fuzzy Syst. 28 (6) (2020) 1096–1109.

[17] A.M. Anter, D. Gupta, O. Castillo, A novel parameter estimation in dynamic model via fuzzy swarm intelligence and chaos theory for faults in wastewater treatment plant, Soft. Comput. 24 (1) (2020) 111–129.

[18] A.M. Anter, Y.S. Moemen, A. Darwish, A.E. Hassanien, Multi-target QSAR modelling of chemo-genomic data analysis based on extreme learning machine, Knowl.-Based Syst. 188 (2020) 104977.

[19] S. Li, H. Chen, M. Wang, A.A. Heidari, S. Mirjalili, Slime mould algorithm: a new method for stochastic optimization, Future Gen. Comput. Syst. 111 (2020) 300–323.

[20] Y. Fan, J. Shao, G. Sun, X. Shao, Proportional–integral–derivative controller design using an advanced lévy-flight salp swarm algorithm for hydraulic systems, Energies 13 (2) (2020) 459.

[21] C. Hu, Z. Li, T. Zhou, A. Zhu, C. Xu, A multi-verse optimizer with levy flights for numerical optimization and its application in test scheduling for network-on-chip, PLoS ONE 11 (12) (2016) e0167341.

[22] H. Ren, J. Li, H. Chen, C. Li, Adaptive levy-assisted salp swarm algorithm: analysis and optimization case studies, Math. Comput. Simul 181 (2021) 380–409.

[23] G. Iacca, V.C. dos Santos Junior, V.V. de Melo, An improved Jaya optimization algorithm with Lévy flight, Expert Syst. Appl. 165 (2021) 113902.

[24] C. Charin, D. Ishak, M.A.A.M. Zainuri, B. Ismail, M.K.M. Jamil, A hybrid of bio-inspired algorithm based on Levy flight and particle swarm optimizations for photovoltaic system under partial shading conditions, Sol. Energy 217 (2021) 1–14.

[25] Y. Zhang, Z. Jin, X. Zhao, Q. Yang, Backtracking search algorithm with Lévy flight for estimating parameters of photovoltaic models, Energy Convers. Manage. 208 (2020) 112615.

[26] A.M. Anter, A.E. Hassanien, D. Oliva, An improved fast fuzzy c-means using crow search optimization algorithm for crop identification in agricultural, Expert Syst. Appl. 118 (2019) 340–354.

[27] M. Al-Ayyoub, A.M. Abu-Dalo, Y. Jararweh, M. Jarrah, M. Al Sa'd, A gpu-based implementations of the fuzzy c-means algorithms for medical image segmentation, J. Supercomput. 71 (8) (2015) 3149–3162.

[28] C. Wang, W. Pedrycz, M. Zhou, Z. Li, Sparse regularization-based fuzzy C-means clustering incorporating morphological grayscale reconstruction and wavelet frames, IEEE Trans. Fuzzy Syst. (2020), https://doi.org/10.1109/TFUZZ.2020.2985930.

[29] J. Miao, X. Zhou, T.Z. Huang, Local segmentation of images using an improved fuzzy C-means clustering algorithm based on self-adaptive dictionary learning, Appl. Soft Comput. 106200 (2020).

[30] D. Kumar, R.K. Agrawal, H. Verma, Kernel intuitionistic fuzzy entropy clustering for MRI image segmentation, Soft. Comput. 24 (6) (2020) 4003–4026.

[31] T. Lei, X. Jia, Y. Zhang, L. He, H. Meng, A.K. Nandi, Significantly fast and robust fuzzy c-means clustering algorithm based on morphological reconstruction and membership filtering, IEEE Trans. Fuzzy Syst. 26 (5) (2018) 3027–3041.

[32] A.M. Anter, S. Bhattacharyya, Z. Zhang, Multi-stage fuzzy swarm intelligence for automatic hepatic lesion segmentation from CT scans, Appl. Soft Comput. 96 (2020) 106677.

[33] IEEE Covid Chest X-ray, URL: https://github. com/ieee8023/covid-chestxray-data set.

[34] Covid19 Radiography. URL: https://www.kaggle.com/tawsifurrahman/covid19-r adiography-database.

[35] COVID-19 Chest X-ray Dataset Initiative. URL: https://github.com/agchung/Fig ure1-COVID-chestxray-dataset.

[36] Radiopaedie, URL: https://radiopaedia.org/.

[37] M.A. ElSoud, A.M. Anter, Computational intelligence optimization algorithm based on meta-heuristic social-spider: case study on CT liver tumor diagnosis, Comput. Intell. 7 (4) (2016) 466–475.

[38] S. Tian, U. Bhattacharya, S. Lu, B. Su, Q. Wang, X. Wei, C.L. Tan, Multilingual scene character recognition with co-occurrence of histogram of oriented gradients, Pattern Recogn. 51 (2016) 125–134.

[39] S. Tiwari, Blur classification using segmentation based fractal texture analysis, Indonesian J. Electr. Eng. Inform. (IJEEI) 6 (4) (2018) 373–384.

[40] E.H. Yuk, S.H. Park, C.S. Park, J.G. Baek, Feature-learning-based printed circuit board inspection via speeded-up robust features and random forest, Appl. Sci. 8 (6) (2018) 932.

[41] M. Wang, C. Wu, L. Wang, D. Xiang, X. Huang, A feature selection approach for hyperspectral image based on modified ant lion optimizer, Knowl.-Based Syst. 168 (2019) 39–48.

[42] Z. Cui, F. Li, W. Zhang, Bat algorithm with principal component analysis, Int. J. Mach. Learn. Cybern. 10 (3) (2019) 603–622.